

Spatially resolved and time-resolved imaging of transport of indirect excitons in high magnetic fields

C. J. Dorow,¹ M. W. Hasling,¹ E. V. Calman,¹ L. V. Butov,¹ J. Wilkes,² K. L. Campman,³ and A. C. Gossard³

¹*Department of Physics, University of California at San Diego, La Jolla, California 92093-0319, USA*

²*School of Physics and Astronomy, Cardiff University, Cardiff, CF24 3AA Wales, United Kingdom*

³*Materials Department, University of California at Santa Barbara, Santa Barbara, California 93106-5050, USA*

(Received 24 May 2017; published 28 June 2017)

We present the direct measurements of magnetoexciton transport. Excitons give the opportunity to realize the high magnetic-field regime for composite bosons with magnetic fields of a few tesla. Long lifetimes of indirect excitons allow the study of kinetics of magnetoexciton transport with time-resolved optical imaging of exciton photoluminescence. We performed spatially, spectrally, and time-resolved optical imaging of transport of indirect excitons in high magnetic fields. We observed that an increasing magnetic field slows down magnetoexciton transport. The time-resolved measurements of the magnetoexciton transport distance allowed for an experimental estimation of the magnetoexciton diffusion coefficient. An enhancement of the exciton photoluminescence energy at the laser excitation spot was found to anticorrelate with the exciton transport distance. A theoretical model of indirect magnetoexciton transport is presented and is in agreement with the experimental data.

DOI: [10.1103/PhysRevB.95.235308](https://doi.org/10.1103/PhysRevB.95.235308)

I. INTRODUCTION

An indirect exciton (IX) is a bosonic (quasi)particle consisting of a bound electron (e) and a hole (h) confined to spatially separated quantum well (QW) layers [Fig. 1(a)]. The spatial separation of the electron and hole reduces their wave-function overlap, leading to IX lifetimes several orders of magnitude longer than those of regular direct excitons. IXs also form oriented dipoles and have repulsive interactions that facilitate disorder screening. The long IX lifetimes and ability to screen disorder enable long-range transport of IXs before recombination with transport distances reaching up to hundreds of micrometers [1–13].

Several transport phenomena have been observed in systems of IXs, including the inner ring in the IX emission pattern [5,8,9,12,14–16], laser-induced IX trapping [17–20], IX localization-delocalization transitions in random [5,8,9], periodic [21,22], and moving [23,24] potentials, IX spin transport [25,26], and coherent IX transport with suppressed scattering [27,28]. Long-range IX transport also has enabled the realization of several excitonic devices including excitonic ramps [1,7,29,30], conveyers [10,13,23,24], and transistors [31–35].

A system of IXs also provides a unique opportunity to study transport of cold bosons in the high magnetic-field regime. Whereas transport of fermions in high magnetic fields has shown remarkable properties [36], studies of bosons in the high magnetic-field regime have remained elusive to experimenters due to the magnitude of the magnetic fields required. The high magnetic-field regime is achieved when the cyclotron energy is comparable to the binding energy of the boson constituents, which requires $B \sim 10^6$ T for atoms. In contrast, the high magnetic-field regime for excitons is achievable in a laboratory, requiring only a few tesla, due to their small masses and binding energies [37]. In addition to enabling the high magnetic-field regime, IXs possess several other advantageous properties for studying transport of cold bosons in high magnetic fields: Long IX lifetimes enable transport distances that are long enough to be observed with optical imaging; IXs can cool to low temperatures below the temperature of quantum degeneracy due to their long

lifetimes and fast energy relaxation in QWs [38]; the density of photoexcited e-h systems can be controlled by the laser excitation, which allows the realization of virtually any LL filling factor.

An exciton in the high magnetic-field regime, a MX [37,39–41], is composed of an electron and a hole in LL states. The MX dispersion is defined by a coupling between the MX center-of-mass motion and the internal structure: An electron and a hole of a MX are forced to travel with the same velocity and produce on each other a Coulomb force that is balanced by the Lorentz force. This causes MXs with momentum k to acquire an in-plane electric dipole $r_{eh} = kl_B^2$ in the direction perpendicular to k , where $l_B = \sqrt{\hbar c / (eB)}$ is the magnetic length. The coupling between r_{eh} and k allows the MX dispersion $E(k)$ to be calculated from the Coulomb potential between the electron and the hole as a function of r_{eh} . At small k , the MX dispersion is parabolic and can be described

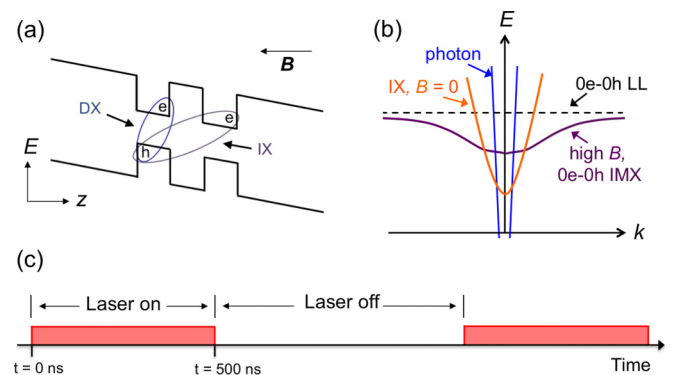


FIG. 1. (a) Coupled QW (CQW) band diagram. (b) Dispersion for IX in a zero magnetic field (orange). Dispersion for indirect magnetoexciton (IMX) formed from e and h in zeroth Landau levels (LLs) in high B (purple). Sum of the e and h LL energies (the black dashed line). Photon dispersion (blue). (c) Schematic of the rectangular laser excitation pulse profile. Time $t = 0$ ns corresponds to the onset of the laser pulse. The pulse width $\tau_{\text{width}} = 500$ ns and pulse period $\tau_{\text{pulse}} = 1.3 \mu\text{s}$.

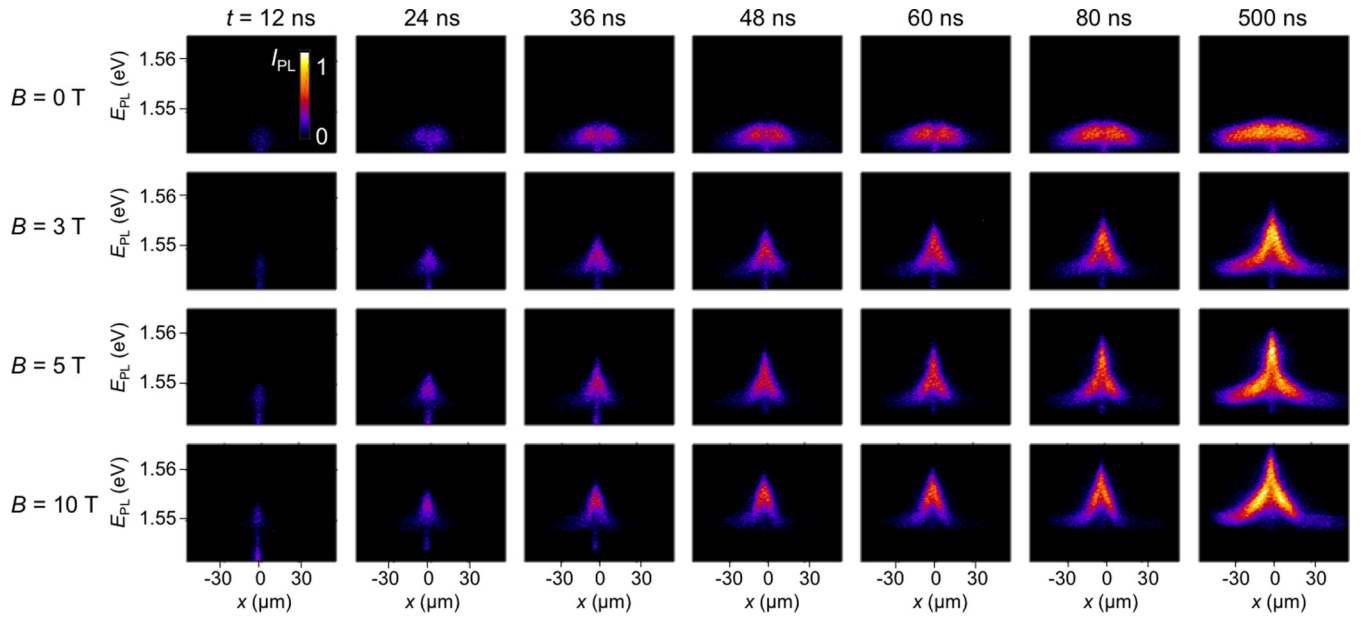


FIG. 2. x -energy IMX PL images taken during the laser excitation pulse. Images are taken for several delay times t after the onset of the laser pulse and several magnetic fields. Each image is integrated over a time window of $\delta t = 4$ ns. $T_{\text{bath}} = 1.5$ K and average $P_{\text{ex}} = 670 \mu\text{W}$ for all data. Laser excitation is centered around $x = 0$.

by an effective MX mass that grows with B . Figure 1(b) shows the transformation of the $1s$ exciton dispersion at $B = 0$ to the 0_e-0_h MX dispersion at high B (MX composed of an electron and hole each in the zeroth LL). Several collective states and transport phenomena have been predicted for gases of MXs including a paired Laughlin liquid [42], an excitonic charge-density-wave state [43], a condensate of MXs [44,45], the exciton Hall effect [46,47], superfluidity [44,45,47,48], and localization [49].

The MX properties can be probed by photoluminescence (PL) techniques. In GaAs QW structures, free two-dimensional (2D) MXs can recombine radiatively when they are composed from electrons and holes at LLs with $N_e = N_h$, where N is the LL number of the electron and hole, their spin projections on the z direction is $J_z = \pm 1$, and their momentum k lies within the intersection between the MX dispersion surface $E_{\text{MX}}(k)$ and the photon cone $E = \hbar kc / \sqrt{\epsilon}$ [blue curve in Fig. 1(b)], called the radiative zone [50–53] (ϵ is the dielectric constant). Free MXs with $N_e \neq N_h$, $J_z = \pm 2$, or k outside the radiative zone remain dark.

In earlier studies of excitons in high magnetic fields, excitons and deexcitons in dense e-h plasmas in single QWs were observed [54,55]. However, short lifetimes of excitons in single QWs did not allow the achievement of low exciton temperatures or long-range exciton transport before recombination. Recently, the transport properties of cold MXs were addressed with IMXs in CQWs by imaging of an IMX emission cloud in cw experiments [56]. In these experiments, long-range transport was evidenced for IMXs composed of electrons and holes in the lowest LLs, however no time-resolved measurement of the IMX cloud expansion directly showing IMX transport was performed. The magnetic-field effects on IX energies [57–62], dispersion relations [37,63–66], and spin states [26,67] have also been studied.

In this paper, we present direct measurements of IX transport in high magnetic fields, achieved with spatially, spectrally, and time-resolved optical imagings.

II. EXPERIMENT

IXs were studied in a $n^+ - i - n^+$ GaAs CQW grown by molecular beam epitaxy [Fig. 1(a)]. The i region is a pair of 8-nm GaAs QWs separated by a 4-nm $\text{Al}_{0.33}\text{Ga}_{0.67}\text{As}$ barrier, all surrounded by 200-nm $\text{Al}_{0.33}\text{Ga}_{0.67}\text{As}$ layers. The spacing between the electron and the hole layers derived from the IX energy shift with applied voltage is $d \sim 11.5$ nm, close to the nominal distance between the QW centers. The n^+ layers are Si-doped GaAs with $n_{\text{Si}} = 5 \times 10^{17} \text{ cm}^{-3}$. The indirect regime where the IX is the lowest-energy state was achieved by applying voltage $V = 1.4$ V across the n^+ layers.

Time-resolved optical imaging using a pulsed laser excitation was performed. IXs were photogenerated with a 658-nm (1.88-eV) laser with a pulse duration of $\tau_{\text{width}} = 500$ ns and a pulse period of $\tau_{\text{pulse}} = 1.3 \mu\text{s}$ with an edge sharpness of ~ 1 ns [Fig. 1(c)]. The rectangular-shaped pulses were realized by a pulse generator driving a semiconductor laser. The period and duty cycle were optimized to allow the IMX PL image to reach equilibrium during the laser excitation and decay between laser pulses. The laser was focused to a $R_0 = 4.5\text{-}\mu\text{m}$ half width at half maximum (HWHM) spot. Images were integrated over 4-ns windows ($\delta t = 4$ ns) and taken for several delay times t after the onset of the laser pulse, defined such that a delay time t corresponds to an image taken during time $t - \delta t$ to t .

The images were captured with the use of a liquid-nitrogen-cooled CCD coupled to a PicoStar HR TauTec time-gated intensifier. The PL was passed through a spectrometer with a resolution of 0.18 meV before entering the intensifier and

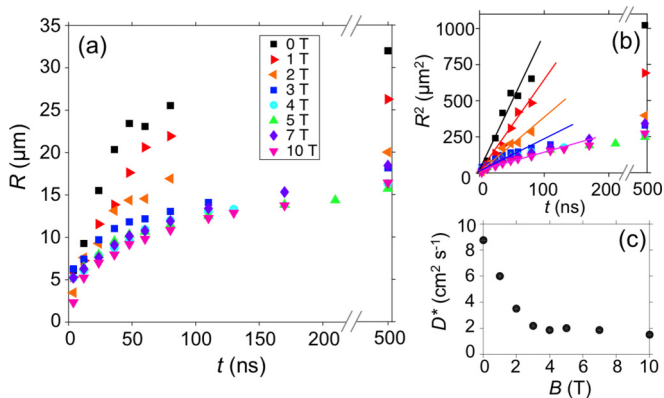


FIG. 3. (a) IMX transport radius R vs delay time t for $B = 0$ –10 T. (b) R^2 vs t for $B = 0$ –10 T. (c) Measured IMX diffusion coefficient vs B (see text). $T_{\text{bath}} = 1.5$ K and average excitation power $P_{\text{ex}} = 670 \mu\text{W}$ for all data.

CCD in order to obtain spectral resolution. The spectrally and time-resolved imaging enables the direct measurement of the evolution of the IX PL intensity and energy as a function of delay time t . All measurements were performed at $T_{\text{bath}} = 1.5$ K with applied magnetic fields up to 10 T oriented perpendicular to the CQW plane.

Figure 2 shows a sample of x -energy images of the IMX PL spanning over a range of delay times t and several magnetic fields. All images in Fig. 2 are taken during the laser excitation ($t < \tau_{\text{width}}$) with the laser centered around $x = 0$. The magnetic field has an effect on both the IMX transport distance and the energy; the IMX PL signal morphs to a chevron shape with increasing magnetic field. The expansion of the IMX cloud due to IMX transport is observed directly over time and is characterized by a transport radius R , where R is the HWHM of the spectrally integrated IMX emission. Figure 3(a) shows R vs t for each B . With increasing magnetic field, the IMX transport slows down as seen by the flattening of the slope of the curves $R(t)$ with increasing B .

The slowing down of the IMX transport with increasing B is consistent with the IMX effective mass $M(B)$ enhancement. The latter was observed in earlier experiments [64] and derived in earlier theoretical works [37,65,66]. For instance, it was shown that for the IXs in the GaAs CQW, the application of magnetic-field $B = 10$ T results in the enhancement of $M(B)$ by more than five times [37,64–66]. The IMX mass increase affects both the IMX diffusion and the drift since both the exciton diffusion coefficient D and the exciton mobility μ_x are inversely proportional to the mass [68].

The time-resolved imaging of the IMX cloud expansion enables the estimation of IMX transport characteristics. Figure 3(b) shows that, at the initial delay times, R^2 grows nearly linearly with t . Fitting to the slope by $R^2 \sim R_0^2 + D^*t$ gives an estimate of the effective IX diffusion coefficient D^* , which encapsulates both D and μ_x . A quantitative description of D^* is presented in Sec. III. The values of D^* estimated from this experiment are plotted in Fig. 3(c) and are found to decrease with increasing B , quantifying the IMX transport suppression in high B .

We note also that at long delays the slope of $R^2(t)$ reduces. This is consistent with the theory (Sec. III) and is mainly due

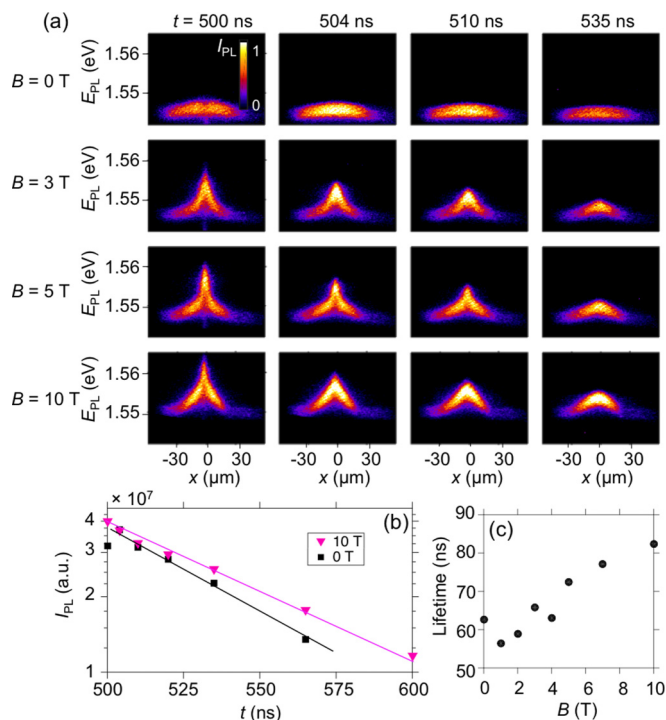


FIG. 4. IMX decay after laser pulse termination. (a) x -energy IMX PL images taken during a laser pulse ($t = 500$ ns) and after a laser pulse termination ($t > 500$ ns) for several magnetic fields. (b) Total IMX PL intensity (integrated over all x 's and E 's) vs t for $B = 0$ and 10 T. (c) Measured IMX lifetime vs B . $T_{\text{bath}} = 1.5$ K and average $P_{\text{ex}} = 670 \mu\text{W}$ for all data.

to the finite IX lifetime τ , which limits the exciton transport distance by $R \sim \sqrt{D\tau}$.

The ring-shaped exciton PL due to the PL intensity suppression in the region of the laser excitation spot [5,8,9,12,14–16] around $x = 0$ can be seen during the excitation pulse at long delay times when the conditions become similar to the cw excitation considered in earlier works [56], see, e.g., the $t = 500$ -ns, $B = 0$ image in Fig. 2. However, the ring contrast is smaller in the presented time-resolved experiments than in the earlier cw experiments [56] because the laser excitation was more tightly focused in the cw experiments [56].

The kinetics of the IMX decay after the laser pulse termination is presented in Fig. 4. The decay of the IMX PL intensity after the laser pulse termination can be fit to extract the IMX lifetime as seen in Fig. 4(b), where I_{PL} is the total PL intensity integrated over all energies and x . The IMX lifetime is observed to increase with B [Fig. 4(c)], in agreement with the earlier spatially integrated measurements [59]. The IMX dispersion flattening with increasing B [Fig. 1(b)] reduces the energy width of the radiative zone, thus contributing to the IMX lifetime increase.

The evolution of the IMX PL energy is presented in Fig. 5. Figures 5(a) and 5(b) show the IMX average PL energy $M_1(x) = \int EI(x,E)dE / \int I(x,E)dE$ as a function of delay time t for $B = 5$ T. During the laser excitation pulse, the IMX PL blueshifts over time [Fig. 5(a)]. This can be explained as follows. IMXs are oriented dipoles with a built-in dipole moment ed and therefore interact repulsively. Thus, IMX energy increases with density. IMXs are photoexcited, and

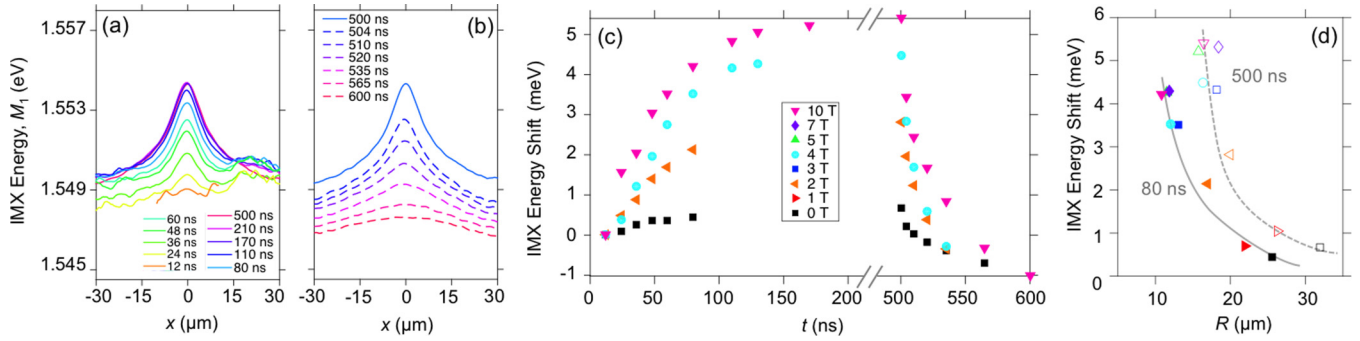


FIG. 5. IMX energy presented by the first moment of IMX PL $M_1(x)$ for different delay times (a) during the laser pulse and (b) after the laser pulse. $B = 5$ T. (c) IMX energy shift $M_1(t) - M_1(t = 12 \text{ ns})$ at $x = 0$. (d) IMX transport radius R vs IMX energy shift at $x = 0$ for several B 's at two delays: $t = 80$ ns (filled markers) and $t = 500$ ns (open markers). $T_{\text{bath}} = 1.5$ K and average $P_{\text{ex}} = 670 \mu\text{W}$ for all data.

their density grows with time after the onset of laser excitation, leading to a blueshift of the IMX emission line with time. Similarly, the IMX emission line redshifts after the laser excitation is terminated [dashed lines in Fig. 5(b)], and this is due to a decrease in IMX density and therefore a reduction of repulsive IMX-IMX interaction.

For all delay times, $M_1(x)$ is peaked in the laser excitation region around $x = 0$ and reduces with x , following the reducing IMX density away from the laser excitation spot. Figure 5(c) presents the IMX energy shift $M_1(t) - M_1(t = 12 \text{ ns})$ at $x = 0$ (here the IMX energy is plotted relative to the IMX energy at $t = 12$ ns to compensate for the IMX diamagnetic energy shift [56]). A larger blueshift is observed over time for higher magnetic fields [Fig. 5(c)]. This is due to the IMX density accumulation in the excitation spot region originating from the suppression of IMX transport away from the excitation spot with increasing B [Fig. 3(a)]. The suppression of IMX transport and, as a result, IMX density accumulation near the IMX generation site, is stronger with increasing magnetic fields. This effect also is presented in Fig. 5(d) showing that the IMX transport distance R anticorrelates with the IMX shift at $x = 0$.

Figure 6(a) shows the laser excitation power P_{ex} dependence of the evolution of the IMX transport distance. The IMX density is controlled with P_{ex} ; higher P_{ex} corresponds to higher IMX density. At low densities ($P_{\text{ex}} = 25 \mu\text{W}$), the radius of the IMX emission cloud is essentially that of the laser excitation spot, indicating that IMX transport is suppressed. In contrast, at high densities ($P_{\text{ex}} = 670 \mu\text{W}$), the IMX cloud extends well beyond the laser excitation spot due to long-range IMX transport [Fig. 6(a)]. The different IMX transport distances between the two densities are understood in terms of disorder screening. At low densities, IMXs are localized in the disorder potential of the sample. However, since IMXs interact repulsively, at higher densities, they effectively screen the disorder potential and become delocalized, and long-range IMX transport is observed at higher excitation powers.

Figure 6(b) shows that the IMX energy shift is stronger for the higher laser power. A higher repulsive IMX interaction at higher IMX densities contributes to this. We note however that the population of higher LL states also can contribute to a larger blueshift. An investigation of the kinetics of individual LL states is the subject of future work.

III. THEORY

A model based on exciton transport and thermalization is used to simulate the IMX kinetics in high magnetic fields. We solved the following set of coupled equations for the IMX density n and temperature T ,

$$\frac{\partial n}{\partial t} = \nabla[D\nabla n + \mu_x n \nabla(u_0 n)] + \Lambda - \frac{n}{\tau}, \quad (1)$$

$$\frac{\partial T}{\partial t} = S_{\text{pump}} - S_{\text{phonon}}. \quad (2)$$

Here, ∇ is the 2D ∇ operator using cylindrical symmetry. The first and second terms in square brackets in Eq. (1) describe IMX diffusion and drift currents, respectively. The latter originates from the repulsive dipolar interactions and is approximated by $u_0 = 4\pi e^2 d/\epsilon$ [9]. The diffusion coefficient

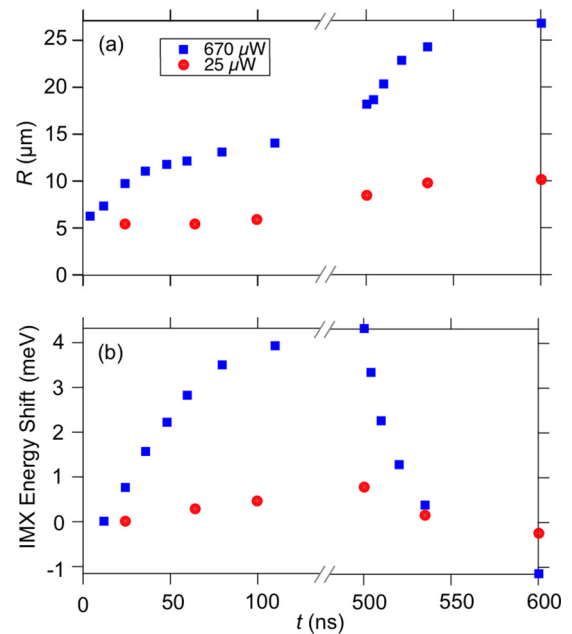


FIG. 6. Laser excitation power dependence. (a) IMX transport radius R vs t for average laser excitation powers $P_{\text{ex}} = 25$ and $670 \mu\text{W}$. (b) IMX energy shift at $x = 0$ vs t for $P_{\text{ex}} = 25$ and $670 \mu\text{W}$. $T_{\text{bath}} = 1.5$ K and $B = 3$ T for all data.

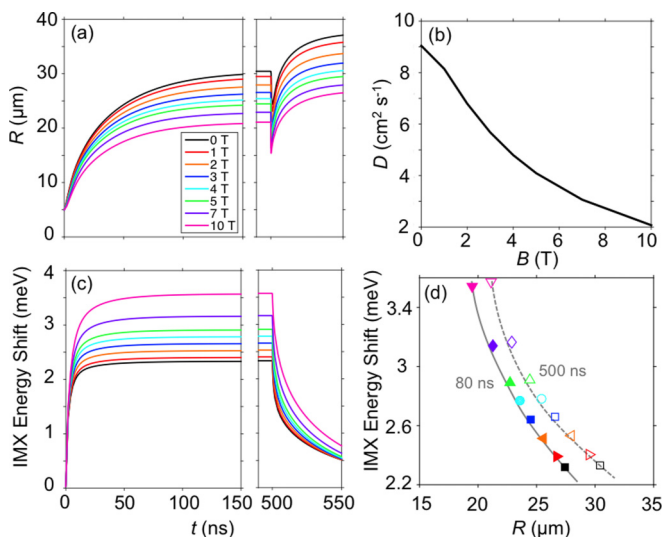


FIG. 7. (a) Calculated IMX transport distance R vs delay time t . (b) Spatially averaged diffusion coefficient D vs B for $t = 10$ ns. (c) Calculated IMX energy shift at $x = 0$ vs t . (d) IMX energy shift at $x = 0$ vs R for $t = 80$ ns (filled markers) and $t = 500$ ns (open markers).

$D(n, T, M)$ is inversely proportional to the IMX effective mass $M(B)$ and describes the magnetic-field-induced reduction in IMX transport. D also accounts for the screening of the random QW disorder potential by IMXs [8,9,68]. The mobility μ_x is given by $\mu_x = D(e^{T_0/T} - 1)/(k_B T_0)$ where $T_0 = \pi \hbar^2 n / [2M(B)k_B]$ is the quantum degeneracy temperature. The IMX generation rate Λ has a Gaussian profile with the same width as the laser excitation beam. τ is the IMX optical lifetime. The thermalization Eq. (2) describes heating of excitons by nonresonant photoexcitation $S_{\text{pump}}(T_0, T)$ and cooling via interaction with bulk longitudinal acoustic phonons $S_{\text{phonon}}(T_0, T)$. The emission intensity is extracted from n/τ . Expressions for D , S_{pump} , S_{phonon} , and τ can be found in Ref. [9].

The magnetic-field dependence enters Eqs. (1) and (2) via D and T_0 since both depend on $M(B)$. In addition, τ is given by the single $k = 0$ IMX lifetime $\tau_r(B)$ divided by the fraction of IMXs that are inside the radiative zone. The radiative zone is the region in momentum space contained within the intersection between the photon and the exciton dispersion surfaces, the latter being a function of $M(B)$ [Fig. 1(b)]. The increase in $M(B)$ decreases the energy width of the radiative zone, which lowers its occupation and enhances τ . At the same time, the magnetic field shrinks the in-plane Bohr radius, increasing the probability of electron-hole recombination and thus decreasing τ . $M(B)$ and $\tau_r(B)$ were determined in Refs. [65,66] by calculating eigenstates of the Hamiltonian describing the relative motion of a Coulomb bound electron-hole pair using the multisublevel approach [65,66,69].

The experimental data in Fig. 4(c) show the IMX lifetime increasing with B . This indicates that the reduction of the radiative zone is the dominant effect in determining the IMX lifetime. In contrast, the calculated τ decreases with increasing B at temperatures below about 2 K and increases with increasing B at higher temperatures [66]. This discrepancy

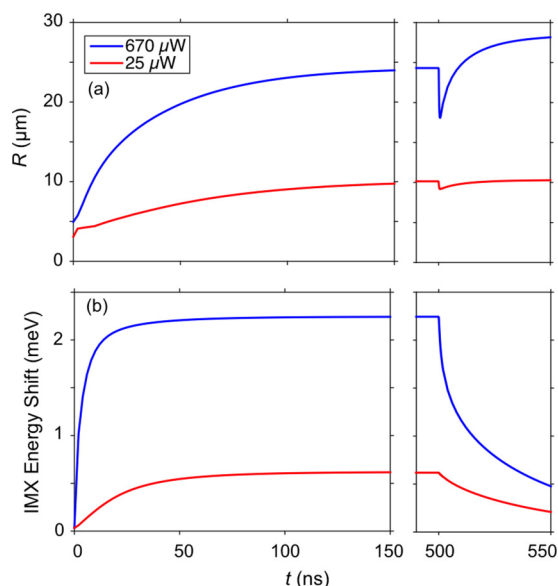


FIG. 8. (a) Calculated IMX transport distance R and (b) IMX energy shift at $x = 0$ vs delay time t for $P_{\text{ex}} = 25 \mu\text{W}$ (red) and $670 \mu\text{W}$ (blue).

is likely due to the nonparabolicity of the exciton dispersion which was not included in the estimates [66].

Figures 7(a) and 7(c) show the calculated IMX transport distance and energy shift vs delay time for all magnetic fields. The theoretical simulations are in qualitative agreement with the experimental data. The spatially averaged diffusion coefficient D plotted in Fig. 7(b) exhibits a similar dependence as the experimentally extracted D^* in Fig. 3(c). The evolution of the IMX density $n(r, t)$ from Eq. (1) shows that $D^* \approx D + \mu_x n u_0$. The experimentally measured expansion of the exciton PL cloud is determined by both exciton drift and diffusion, whereas the simulations allow separately addressing exciton diffusion. Quantitative differences between the experimental data [Fig. 3(c)] and the simulations [Fig. 7(b)] include a faster saturation behavior in the experiment. The quantitative differences partly are related to the difference between D and D^* , however the approximations used in the model, in particular neglecting the population kinetics of higher LL IMX states, imply that a more accurate model is needed for quantitative comparisons with experiment. The theoretical model also shows a higher blueshift in IMX PL energy at the origin due to the suppression of IMX transport at higher magnetic fields [compare Fig. 5(d) to Fig. 7(d)].

Figures 8(a) and 8(b) show the calculated IMX transport distance and energy shift vs delay time for high and low laser excitation powers at $B = 3$ T. The calculations show longer transport distances and higher-energy shifts at higher laser power, consistent with the experiment [compare Fig. 6 to Fig. 8].

We note that IX PL intensity is suppressed in the excitation spot region during the excitation pulse due to the laser-induced heating of IXs resulting in a lowering of the radiative zone occupation [5,8,9,16,56]. After the excitation pulse termination, IXs cool down, and the IX PL intensity increases at the excitation spot region a few nanoseconds after the excitation

pulse ends [9]. This results in the apparent reduction kink in R [Fig. 7(a)] (the kink is not observed in the experiment within the experimental resolution). An enhancement of R after the excitation pulse termination also is observed in the simulations [Figs. 7(a) and 8(a)], consistent with the experiment [compare Fig. 6(a) to Fig. 8(a)]. This enhancement of the IMX transport distance is consistent with a better screening of the QW disorder potential by colder IMXs. Inclusion of the population kinetics of higher LL IMX states and their effect on R is the subject of future work.

IV. SUMMARY

Transport of IMXs in high magnetic fields was studied with time-resolved optical imaging. Slower IMX transport was observed at higher magnetic fields. This was attributed to the exciton effective mass increase with magnetic field. An enhancement of the IMX energy at the laser excitation spot was

found to anticorrelate with the IMX transport distance. This was attributed to an accumulation of repulsively interacting IMXs near their generation site due to the suppression of IMX transport at high magnetic fields. Faster IMX transport was observed at a higher laser excitation power. This was attributed to IMX delocalization from the disorder potential due to disorder screening at higher IMX densities. A theoretical model of IMX transport is in agreement with the experiment.

ACKNOWLEDGMENTS

These studies of indirect excitons were supported by NSF Grant No. 1640173 and NERC, a subsidiary of SRC, through the SRC-NRI Center for Excitonic Devices and by NSF Grant No. 1407277. C.J.D. was supported by the NSF Graduate Research Fellowship Program under Grant No. DGE-1144086. J.W. was supported by the EPSRC (Grant No. EP/L022990/1).

-
- [1] M. Hagn, A. Zrenner, G. Böhm, and G. Weimann, *Appl. Phys. Lett.* **67**, 232 (1995).
- [2] L. V. Butov and A. I. Filin, *Phys. Rev. B* **58**, 1980 (1998).
- [3] V. Negoita, D. W. Snoke, and K. Eberl, *Phys. Rev. B* **60**, 2661 (1999).
- [4] A. V. Larionov, V. B. Timofeev, J. Hvam, and K. Soerensen, *Zh. Eksp. Teor. Fiz.* **117**, 1255 (2000) [*J. Exp. Theor. Phys.* **90**, 1093 (2000)].
- [5] L. V. Butov, A. C. Gossard, and D. S. Chemla, *Nature (London)* **418**, 751 (2002).
- [6] Z. Vörös, R. Balili, D. W. Snoke, L. Pfeiffer, and K. West, *Phys. Rev. Lett.* **94**, 226401 (2005).
- [7] A. Gärtner, A. W. Holleitner, J. P. Kotthaus, and D. Schuh, *Appl. Phys. Lett.* **89**, 052108 (2006).
- [8] A. L. Ivanov, L. E. Smallwood, A. T. Hammack, S. Yang, L. V. Butov, and A. C. Gossard, *Europhys. Lett.* **73**, 920 (2006).
- [9] A. T. Hammack, L. V. Butov, J. Wilkes, L. Mouchliadis, E. A. Muljarov, A. L. Ivanov, and A. C. Gossard, *Phys. Rev. B* **80**, 155331 (2009).
- [10] S. Lazić, P. V. Santos, and R. Hey, *Phys. E* **42**, 2640 (2010).
- [11] M. Alloing, A. Lemaître, and F. Dubin, *Europhys. Lett.* **93**, 17007 (2011).
- [12] M. Alloing, A. Lemaître, E. Galopin, and F. Dubin, *Phys. Rev. B* **85**, 245106 (2012).
- [13] S. Lazić, A. Violante, K. Cohen, R. Hey, R. Rapaport, and P. V. Santos, *Phys. Rev. B* **89**, 085313 (2014).
- [14] M. Stern, V. Garmider, E. Segre, M. Rappaport, V. Umansky, Y. Levinson, and I. Bar-Joseph, *Phys. Rev. Lett.* **101**, 257402 (2008).
- [15] A. L. Ivanov, E. A. Muljarov, L. Mouchliadis, and R. Zimmermann, *Phys. Rev. Lett.* **104**, 179701 (2010).
- [16] Y. Y. Kuznetsova, J. R. Leonard, L. V. Butov, J. Wilkes, E. A. Muljarov, K. L. Campman, and A. C. Gossard, *Phys. Rev. B* **85**, 165452 (2012).
- [17] A. T. Hammack, M. Griswold, L. V. Butov, L. E. Smallwood, A. L. Ivanov, and A. C. Gossard, *Phys. Rev. Lett.* **96**, 227402 (2006).
- [18] A. T. Hammack, L. V. Butov, L. Mouchliadis, A. L. Ivanov, and A. C. Gossard, *Phys. Rev. B* **76**, 193308 (2007).
- [19] A. V. Gorbunov, V. B. Timofeev, and D. A. Demin, *Pis'ma Zh. Eksp. Teor. Fiz.* **94**, 877 (2011) [*JETP Lett.* **94**, 800 (2011)].
- [20] M. Alloing, A. Lemaître, E. Galopin, and F. Dubin, *Sci. Rep.* **3**, 1578 (2013).
- [21] M. Remeika, J. C. Graves, A. T. Hammack, A. D. Meyertholen, M. M. Fogler, L. V. Butov, M. Hanson, and A. C. Gossard, *Phys. Rev. Lett.* **102**, 186803 (2009).
- [22] M. Remeika, M. M. Fogler, L. V. Butov, M. Hanson, and A. C. Gossard, *Appl. Phys. Lett.* **100**, 061103 (2012).
- [23] A. G. Winbow, J. R. Leonard, M. Remeika, Y. Y. Kuznetsova, A. A. High, A. T. Hammack, L. V. Butov, J. Wilkes, A. A. Guenther, A. L. Ivanov, M. Hanson, and A. C. Gossard, *Phys. Rev. Lett.* **106**, 196806 (2011).
- [24] M. W. Hasling, Y. Y. Kuznetsova, P. Andreakou, J. R. Leonard, E. V. Calman, C. J. Dorow, L. V. Butov, M. Hanson, and A. C. Gossard, *J. Appl. Phys.* **117**, 023108 (2015).
- [25] J. R. Leonard, Y. Y. Kuznetsova, S. Yang, L. V. Butov, T. Ostatnický, A. Kavokin, and A. C. Gossard, *Nano Lett.* **9**, 4204 (2009).
- [26] A. A. High, A. T. Hammack, J. R. Leonard, S. Yang, L. V. Butov, T. Ostatnický, M. Vladimirova, A. V. Kavokin, T. C. H. Liew, K. L. Campman, and A. C. Gossard, *Phys. Rev. Lett.* **110**, 246403 (2013).
- [27] A. A. High, J. R. Leonard, A. T. Hammack, M. M. Fogler, L. V. Butov, A. V. Kavokin, K. L. Campman, and A. C. Gossard, *Nature (London)* **483**, 584 (2012).
- [28] M. Alloing, M. Beian, M. Lewenstein, D. Fuster, Y. González, L. González, R. Combescot, M. Combescot, and F. Dubin, *Europhys. Lett.* **107**, 10012 (2014).
- [29] J. R. Leonard, M. Remeika, M. K. Chu, Y. Y. Kuznetsova, A. A. High, L. V. Butov, J. Wilkes, M. Hanson, and A. C. Gossard, *Appl. Phys. Lett.* **100**, 231106 (2012).
- [30] C. J. Dorow, Y. Y. Kuznetsova, J. R. Leonard, M. K. Chu, L. V. Butov, J. Wilkes, M. Hanson, and A. C. Gossard, *Appl. Phys. Lett.* **108**, 073502 (2016).
- [31] A. A. High, A. T. Hammack, L. V. Butov, M. Hanson, and A. C. Gossard, *Opt. Lett.* **32**, 2466 (2007).
- [32] A. A. High, E. E. Novitskaya, L. V. Butov, M. Hanson, and A. C. Gossard, *Science* **321**, 229 (2008).

- [33] G. Grosso, J. Graves, A. T. Hammack, A. A. High, L. V. Butov, M. Hanson, and A. C. Gossard, *Nat. Photonics* **3**, 577 (2009).
- [34] Y. Y. Kuznetsova, M. Remeika, A. A. High, A. T. Hammack, L. V. Butov, M. Hanson, and A. C. Gossard, *Opt. Lett.* **35**, 1587 (2010).
- [35] P. Andreakou, S. V. Poltavtsev, J. R. Leonard, E. V. Calman, M. Remeika, Y. Y. Kuznetsova, L. V. Butov, J. Wilkes, M. Hanson, and A. C. Gossard, *Appl. Phys. Lett.* **104**, 091101 (2014).
- [36] For reviews, see *Perspectives in Quantum Hall Effects*, edited by S. Das Sarma and A. Pinczuk (Wiley, New York, 1997); H. L. Störmer, D. C. Tsui, and A. C. Gossard, *Rev. Mod. Phys.* **71**, S298 (1999).
- [37] Y. E. Lozovik, I. V. Ovchinnikov, S. Y. Volkov, L. V. Butov, and D. S. Chemla, *Phys. Rev. B* **65**, 235304 (2002).
- [38] L. V. Butov, A. L. Ivanov, A. Imamoglu, P. B. Littlewood, A. A. Shashkin, V. T. Dolgoplov, K. L. Campman, and A. C. Gossard, *Phys. Rev. Lett.* **86**, 5608 (2001).
- [39] L. P. Gor'kov and I. E. Dzyaloshinskii, *Zh. Eksp. Teor. Fiz.* **53**, 717 (1967) [*Sov. Phys. JETP* **26**, 449 (1968)].
- [40] I. V. Lerner and Yu. E. Lozovik, *Zh. Eksp. Teor. Fiz.* **78**, 1167 (1978) [*Sov. Phys. JETP* **51**, 588 (1980)].
- [41] C. Kallin and B. I. Halperin, *Phys. Rev. B* **30**, 5655 (1984).
- [42] D. Yoshioka and A. H. MacDonald, *J. Phys. Soc. Jpn.* **59**, 4211 (1990).
- [43] X. M. Chen and J. J. Quinn, *Phys. Rev. Lett.* **67**, 895 (1991).
- [44] Y. Kuramoto and C. Horie, *Solid State Commun.* **25**, 713 (1978).
- [45] I. V. Lerner and Yu. E. Lozovik, *Zh. Eksp. Teor. Fiz.* **80**, 1488 (1981) [*Sov. Phys. JETP* **53**, 763 (1981)].
- [46] A. B. Dzyubenko and Y. E. Lozovik, *Fiz. Tverd. Tela* **26**, 1540 (1984) [*Sov. Phys. Solid State* **26**, 938 (1984)].
- [47] D. Paquet, T. M. Rice, and K. Ueda, *Phys. Rev. B* **32**, 5208 (1985).
- [48] A. Imamoglu, *Phys. Rev. B* **54**, 14285(R) (1996).
- [49] P. I. Arseyev and A. B. Dzyubenko, *Phys. Rev. B* **52**, R2261 (1995).
- [50] J. Feldmann, G. Peter, E. O. Göbel, P. Dawson, K. Moore, C. Foxon, and R. J. Elliott, *Phys. Rev. Lett.* **59**, 2337 (1987).
- [51] E. Hanamura, *Phys. Rev. B* **38**, 1228 (1988).
- [52] L. C. Andreani, F. Tassone, and F. Bassani, *Solid State Commun.* **77**, 641 (1991).
- [53] M. Z. Maialle, E. A. de Andrada e Silva, and L. J. Sham, *Phys. Rev. B* **47**, 15776 (1993).
- [54] L. V. Butov, V. D. Kulakovskii, and E. I. Rashba, *Pis'ma Zh. Eksp. Teor. Fiz.* **53**, 104 (1991) [*JETP Lett.* **53**, 109 (1991)].
- [55] L. V. Butov, V. D. Kulakovskii, G. E. W. Bauer, A. Forchel, and D. Grützmacher, *Phys. Rev. B* **46**, 12765 (1992).
- [56] Y. Y. Kuznetsova, C. J. Dorow, E. V. Calman, L. V. Butov, J. Wilkes, E. A. Muljarov, and K. L. Campman, A. C. Gossard, *Phys. Rev. B* **95**, 125304 (2017).
- [57] L. V. Butov, A. Zrenner, G. Abstreiter, A. V. Petinova, and K. Eberl, *Phys. Rev. B* **52**, 12153 (1995).
- [58] A. B. Dzyubenko and A. L. Yablonskii, *Phys. Rev. B* **53**, 16355 (1996).
- [59] L. V. Butov, A. A. Shashkin, V. T. Dolgoplov, K. L. Campman, and A. C. Gossard, *Phys. Rev. B* **60**, 8753 (1999).
- [60] L. V. Butov, A. Imamoglu, K. L. Campman, and A. C. Gossard, *Zh. Eksp. Teor. Fiz.* **119**, 301 (2001) [*J. Exp. Theor. Phys.* **92**, 260 (2001)].
- [61] K. Kowalik-Seidl, X. P. Vögele, F. Seilmeier, D. Schuh, W. Wegscheider, A. W. Holleitner, and J. P. Kotthaus, *Phys. Rev. B* **83**, 081307(R) (2011).
- [62] G. J. Schinner, J. Repp, K. Kowalik-Seidl, E. Schubert, M. P. Stallhofer, A. K. Rai, D. Reuter, A. D. Wieck, A. O. Govorov, A. W. Holleitner, and J. P. Kotthaus, *Phys. Rev. B* **87**, 041303(R) (2013).
- [63] Y. E. Lozovik and A. M. Ruvinskii, *Zh. Eksp. Teor. Fiz.* **112**, 1791 (1997) [*J. Exp. Theor. Phys.* **85**, 979 (1997)].
- [64] L. V. Butov, C. W. Lai, D. S. Chemla, Y. E. Lozovik, K. L. Campman, and A. C. Gossard, *Phys. Rev. Lett.* **87**, 216804 (2001).
- [65] J. Wilkes and E. A. Muljarov, *New J. Phys.* **18**, 023032 (2016).
- [66] J. Wilkes and E. A. Muljarov, *Superlattices Microstruct.* **108**, 32 (2017).
- [67] A. V. Gorbunov and V. B. Timofeev, *Solid State Commun.* **157**, 6 (2013).
- [68] A. L. Ivanov, *Europhys. Lett.* **59**, 586 (2002).
- [69] K. Sivalertporn, L. Mouchliadis, A. L. Ivanov, R. Philp, and E. A. Muljarov, *Phys. Rev. B* **85**, 045207 (2012).